# A power-adaptive neuron model and circuit implementation

Xiaosong Li[1,2], Jingru Sun[1,2*†], Yichuang Sun[3†], Jiliang Zhang[4†]

[1]College of Computer Science and Electronic Engineering, Hunan University, Changsha, 410082, China.
[2]Chongqing Research Institute, Hunan University, Chongqing, 401120, China.
[3]School of Engineering and Computer Science, University of Hertfordshire, Hatfield AL10 9AB, UK.
[4]College of Integrated Circuits, Hunan University, Changsha, 410082, China.

*Corresponding author(s). E-mail(s): jt_sunjr@hnu.edu.cn;
Contributing authors: liguangbi@hnu.edu.cn; y.sun@herts.ac.uk;
zhangjiliang@hnu.edu.cn;
†These authors contributed equally to this work.

**Abstract**

Regarding the performance degradation and battery life issues faced by mobile smart devices during low energy supply. This article thoroughly explores the strategies employed by biological neurons to stabilize spike emission frequency and reduce power consumption during low energy supply, as well as the characteristics of myelin sheath in reducing power consumption. A power-adaptive neuron (PAN) model and its corresponding power-adaptive neuron circuit system (PANCS) are proposed, which adaptively adjust power consumption according to energy supply conditions. Simulation and practical experiments both indicate that PANCS has acquired power-adaptive adjustment capability (PAAC), maintaining stable spike emission frequency when the system is under insufficient energy supply. This ability increases with the degree of myelination of PANCS. Power consumption analysis indicates that both PAAC and myelination lead to a reduction in power consumption for PANCS when energy supply is insufficient. Noise experiments demonstrate that the efficacy of PAAC entails sacrificing the robustness of PANCS, and myelination cannot reverse the decrease in robustness.

Research findings of this paper endow neural morphology networks with the ability to adaptively adjust power consumption according to energy supply conditions to cope with extreme situations, providing new insights for the development of AI.

**Keywords:** Neurodynamics, Myelin sheath, Memristor, Neuromorphic networks, Robotics, Biomimetic neuronal circuits

# 1 Introduction

Mobile smart devices, represented by intelligent robots, inevitably experience significant performance degradation when the remaining battery energy is insufficient. How to stabilize performance and reduce power consumption has become a widely recognized hot topic in the industry [1, 2]. Brain is currently recognized as the most energy-efficient intelligent carrier. Drawing inspiration from its structure and computational methods has become a primary source of ideas for reducing the power consumption of AI algorithms [3, 4]. Brain possesses a unique mechanism whereby neurons can adaptively reduce energy consumption and maintain a basic discharge frequency to ensure the brain's basic operation when adenosine triphosphate (ATP) supply is insufficient due to starvation, thereby increasing the chances of survival [5, 6]. From a structural and operational perspective, the neural morphology network is one of the AI networks closest to the brain. Analyzing the aforementioned brain mechanisms and incorporating them into the design of neural morphology networks can help address the aforementioned issues.

Supply and consumption strategies of energy strongly sculpt information encoding in the brain throughout evolution. Human brain constitutes less than 2% of the body mass, yet it consumes approximately 20% of the total calorie intake, with 50% of the energy being utilized by the cortex [7]. Cost of excitatory synaptic currents and action potentials (AP) is particularly high, accounting for approximately 57% and 23% of the gray matter electrical signaling energy budget, respectively [8, 9]. Majority of ATP is consumed by ion pumps in the reversal of $Na^+$ and $K^+$ concentrations both inside and outside neurons [8, 10–12]. Under natural selection, the brain has evolved an energy-efficient coding strategy to maximize information transmission per unit of energy (i.e., ATP) [13, 14]. During food scarcity, neural networks conserve energy by reducing information processing due to limited ATP resources. In mice, insufficient ATP prompts neurons to alter energy consumption strategies to sustain basic nervous system functions while conserving energy. In drosophila and caenorhabditis elegans, food deprivation deactivates neural pathways involved in long-term memory to conserve energy [15–17]. Adapting energy consumption based on available resources enhances the biological nervous system's endurance, a strategy worth considering in AI network design for improved endurance.

Myelin sheaths are crucial for neuronal activity, allowing for rapid exchange of information between brain regions, which is essential for cognitive function and human

intelligence development [18]. Most importantly, as the degree of myelination of neurons increases, their basic power consumption significantly decreases [19]. Degree of myelination of neurons is positively correlated with the frequency of firing spikes [20]. Neurons with high discharge frequencies inevitably exhibit increased myelination, resulting in reduced power consumption, thereby driving the entire neural system to lower power consumption. Therefore, the function of myelination contributes to reducing AI power consumption and should not be overlooked when designing AI networks.

The foundation of neuromorphic networks lies in the design of biomimetic neuron circuits. Memristors, known for their compactness, low energy use, and integration ease [21–23], embody organelle traits due to their nonlinearity and are thus commonly used in neuron[24, 25], synapses [26–29] circuit designs, Hopfield neural networks [30] or chaotic systems [31–33]. Most prevalent artificial intelligence neuron circuitry relies on the simplistic LIF model design [34, 35]. While the LIF model captures basic spiking phenomena, it fails to represent intricate firing characteristics [36]. Alternatively, the Hodgkin-Huxley (HH) model offers richer dynamics in neuronal circuits [24, 25, 37, 38], providing detailed neuron firing characteristics by adjusting parameters [36, 39]. However, the lack of description regarding the microdynamics behavior of neuronal myelination and power-adaptive adjustment capability (PAAC). Therefore, this paper supplements this description based on the HH model to enhance its dynamics characteristics and to design neuronal circuit nodes accordingly.

This study explores PAAC of biological neurons and the physiological function of myelin sheaths. Their dynamics characteristics are incorporated into HH model, and a power-adaptive neuron (PAN) model is proposed. Based on this, a power-adaptive neuron circuit system (PANCS) is designed, enabling it to acquire both PAAC and myelin sheath biological characteristics. This allows the system to stabilize spike emission frequency when energy supply is insufficient, thereby ensuring the basic functionality of neural system morphology networks and reducing power consumption. Simulation and practical experiments were designed to validate whether PANCS could undergo myelination and possess PAAC, while also exploring the relationship between myelination and PAAC. Power consumption analysis is aimed at verifying the effectiveness of PAAC and myelination in reducing PANCS energy consumption. Noise experiment is conducted to clarify the cost associated with PANCS using PAAC and whether myelination can mitigate this cost.

The rest of this paper is organized as follows. Section II elaborates on the biological principles of PAAC and neuronal myelination, clearly defining the biomimetic focus; Section III involves establishing dynamics models of organelles involved in neuronal PAAC and myelination, along with providing physical alternative design proposals. It integrates the dynamical characteristics of PAAC and myelination into HH model, proposes the PAN model, and presents the design scheme for PANCS; Section IV comprises simulation, power consumption analysis, and noise testing; Section V involves practical experimentation; Section VI is the conclusion, summarizing the paper.

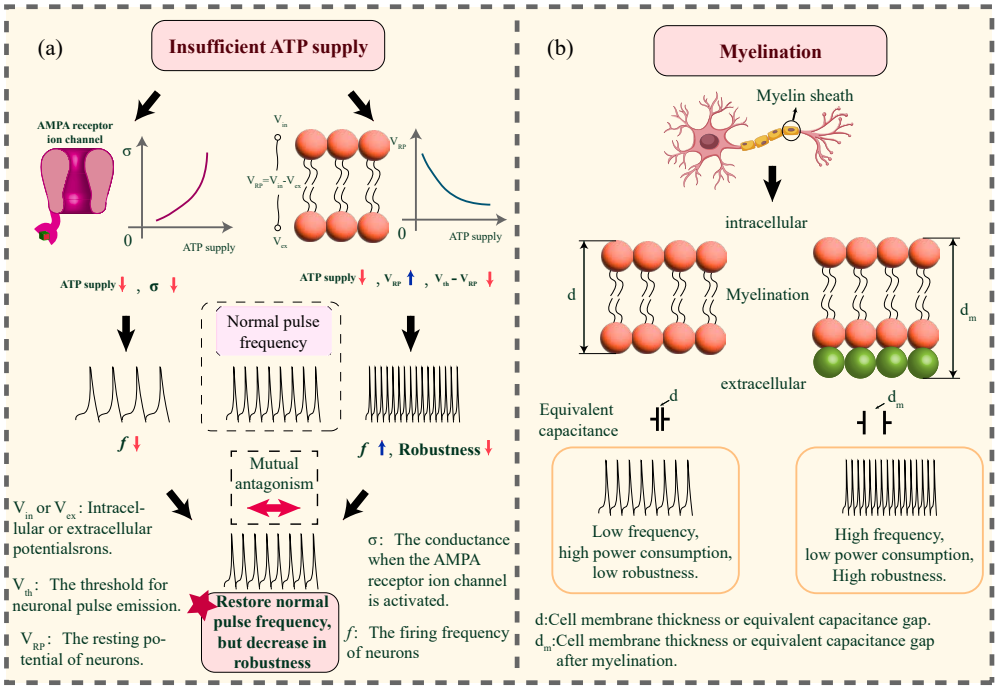


**Fig. 1** (a) Working mechanism of PAAC; (b) Working mechanism of myelination. [5, 40–42]

# 2 Biological foundations

This section primarily introduces the power-adaptive adjustment capability in neurons and the function of myelin sheaths.

## 2.1 power-adaptive adjustment capability in Biological nervous system

The PAAC of the neuron described above aims to stabilize spike firing rates under a low energy supply at the expense of a certain degree of robustness [5]. Two key points need to be met to implement this energy consumption strategy.

Firstly, reducing the conductivity of AMPA receptor ion channels during activation [8, 9], as shown in Fig. 1(a). These channels are regulated by neurotransmitters, and lower conductivity during activation results in fewer inward cations flowing, which can reduce the amount of ATP consumed by the reversal of ion concentration inside and outside the neuron. However, a reduction in the inward flow of cations will prolong the time it takes for the membrane potential to rise from the resting potential to the threshold potential, thereby reducing the spike firing frequency of the neuron. At this point, a second mechanism is needed to maintain the peak firing frequency at normal levels.

Secondly, raising the resting potential, as shown in Fig. 1(a). When there is insufficient ATP supply, neurons do not have enough energy to reverse the $K^+$ concentration inside and outside the cell, forcing the resting potential to increase [8, 10–12]. At this point, the gap between the resting potential and the threshold potential decreases, resulting in shorter accumulation of energy time for firing pulses, leading to an increase in spike firing frequency. At the same time, fewer inward cations are required to trigger pulses, which can also reduce the ATP consumption to reverse the ion concentration difference inside and outside the neuron. When the energy supply is insufficient, the interplay between these two mechanisms ensures that the spike firing frequency is maintained within a stable range, thus guaranteeing the essential operation of the nervous system. However, this adaptive energy consumption mechanism also has its drawbacks. When the gap between the resting potential and the threshold potential decreases, the neuron becomes more active, and the impact of background noise on the firing characteristics of the neuron will be exacerbated.

In conclusion, to implement this PAAC in neuronal circuit nodes, the following three points must be met:

- Firstly, establish a dynamics model based on the biological characteristics of AMPA receptor ion channels and search for suitable physical equivalents to meet the physiological characteristics of channel conductivity fluctuating with membrane potential.
- Secondly, design a reasonable structure to raise the resting potential of the biomimetic neuron circuit when mobile power supply energy is insufficient.
- Thirdly, analyze and summarize the energy consumption mechanism of neurons, and integrate it into the Hodgkin-Huxley model. Optimize this model as the basis for establishing neuronal circuit nodes.

## 2.2 The function of myelin sheath

As shown in Fig. 1(b), the myelin sheath is attached to the surface of the axon cell membrane. With axonal myelination, the thickness of the axon cell membrane (consisting of the myelin sheath layer and the phospholipid bilayer) increases, reducing membrane capacitance. This results in a decrease in the number of inward cations required for neuronal discharge, thereby reducing the ATP consumed by reversing the ion concentration difference inside and outside the neuron and lowering energy consumption [19, 36]. Additionally, the reduction in membrane capacitance also decreases the energy accumulation time time for action potential emission, thereby making the neuron more active and accelerating the pulse emission frequency. Therefore, when establishing neuron models or designing neuronal circuits, considering this myelin sheath functionality is essential.

Myelin sheath growth alters membrane capacitance and permeability, reducing neuronal power consumption and spiking firing rates. In biomimetic neuronal circuit design, capacitors mimic cell membrane capacitance, while resistors simulate non-gated ion channels' permeability. We can replace these components with voltage-controlled resistors and capacitors, enabling them to adjust parameters gradually during spike discharge, mimicking myelin sheath growth [20].

# 3 Mathematical models

In this section, we outline the physiological characteristics of various organelles involved in the operation of neurons and synapses, as well as the physical properties and dynamics equations of physical substitute devices. Specifically, the PANCS is designed strictly according to the three points proposed in Section II. Furthermore, we propose mathematical models that describe the dynamical characteristics of neurons and synapses.

## 3.1 Cell organelles and their physical substitutes

Biological neurons and synapses are intricate systems comprising various organelles with distinct biological traits and spatial arrangements. Aligning physical devices with these organelle traits and interconnecting them according to neural and synaptic structures is pivotal in creating systems that mimic their dynamical characteristics. Action potential firing involves ion channels like $Na^+$, $K^+$, and $Ca^{2+}$, where excitatory and inhibitory synaptic potentials engage various combinations of these channels [36, 43]. Unipolar memristors exhibit nonlinear traits similar to ion channel activation and deactivation, making them suitable physical replacements, as depicted in Fig. 2(a). Their dynamical behavior aligns with $Na^+$ and $Ca^{2+}$ channel properties described in Eq. (1), (2), and (3).

$$V(t) = (R_{off} - x \cdot \Delta R) \cdot i(t), \tag{1}$$

$$\frac{\mathrm{d}x}{\mathrm{d}t} = \begin{cases} q_1 \cdot k_{on}^{b_1} \cdot f(x) \cdot i(t) \cdot \Delta R, & V_{th1} > V(t) \geq V_{th2} \\ 0, \quad V_{th2} > V(t) > V_{th3} \\ q_2 \cdot k_{off}^{b_2} \cdot f(x) \cdot i(t) \cdot \Delta R, & V_{th3} \geq V(t) > V_{th4}, \end{cases} \tag{2}$$

$$f(x) \quad = a \cdot (1 + x)^p, \tag{3}$$

where $V(t)$ represents the voltage across the memristor's two terminals, $R_{off}$ is the high resistance value of the memristor, and $\triangle R$ is the difference between the high resistance value $R_{off}$ and the low resistance value $R_{on}$. The $x$ is the resistance adjustment coefficient, $i(t)$ is the current passing through the memristor and $f(x)$ is the window function. The $q_1$, $q_2$, $a_1$, $a_2$, $k_{off}$, $k_{on}$, $a$, and $p$ are all parameters. $V_{th1}$ and $V_{th2}$ represent the activation threshold and inactivation threshold, respectively.

Compared to $\mathbf{Na}^+$ and $\mathbf{Ca}^{\mathbf{2}+}$ channels, $\mathbf{K}^+$ channels exhibit relatively unique inactivation characteristics, which requires the usage of a different memristor model. The dynamics equation of this memristor is described by Eq. (1), (3), and (4). The $b_1$ and $b_2$ are both parameters, in Eq. (4).

$$\frac{\mathrm{d}x}{\mathrm{d}t} \quad = \quad \begin{cases} q_1 \cdot k_{on}^{b_1} \cdot f(x) \cdot i(t) \cdot \Delta R, & V(t) > V_{th1} \\ 0 \quad , & V_{th1} \geq V(t) > V_{th2} \\ k_{off}^{b_2} \cdot f(x) \cdot i(t)^{q_2} \cdot \Delta R, & V(t) \leq V_{th2}. \end{cases} \tag{4}$$

Fitting AMPAR conductance variations is crucial for simulating adaptive adjustment characteristics of energy consumption strategies. From a physiological standpoint, AMPAR ion channels require the binding of neurotransmitters like glutamate to

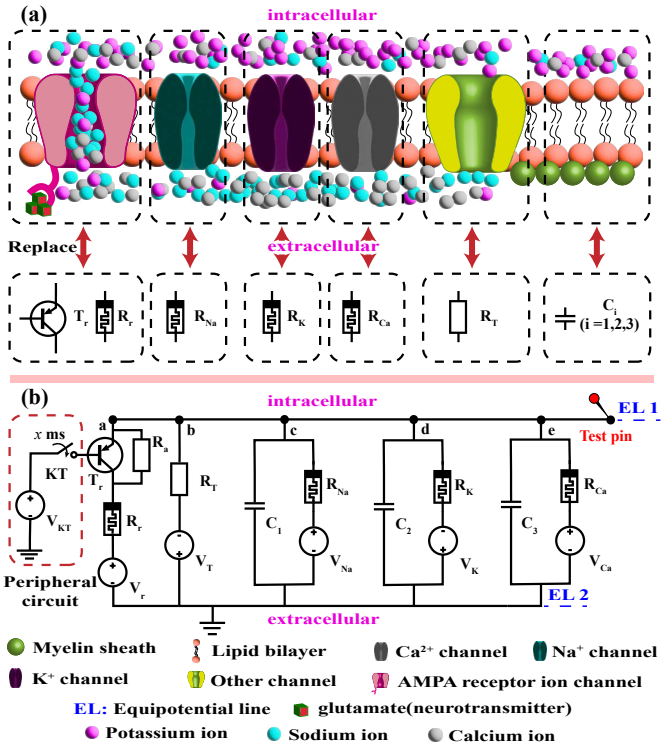


**Fig. 2** (a) Physical substitutes for cell organelles; (b) PANCS.

activate, necessitating three-terminal devices to fulfill its function properly. MOSFETs used as a three-terminal switching device is very suitable here. However, conventional MOSFETs do not possess memristive properties. It is necessary to connect a memristor in series to achieve the physiological function of AMPA receptor ion channels. One key point is that MOSFETs have an extremely high resistance when in the cutoff state, making it difficult for small variations in the resting potential of the neuronal circuit to transmit to the memristor connected in series with it effectively. As a result, the memristor can follow changes in the resting potential to achieve variations in its resistance, which simulates the conductivity changes of AMPA receptor ion channels. Therefore, as shown in Fig. 2(b), it is necessary to use a large resistor in parallel with MOSFETs, followed by the series connection of a memristor, to amplify the memristor's ability to capture changes in the resting potential.

AMPAR can be substituted by the structure depicted in branch '$a$' of Fig. 2(b). The memristor $R_r$ adjusts its conductance in response to biomimetic neuronal membrane potential (MP) changes within a specific range, unaffected by action potentials, described by dynamics characteristics in Eq. (1), (2), and (3). To sensitively adjust the resistance value of $R_r$ during MP fluctuations and ensure that the total conductance of the '$a$' branch remains at a low level in the neuronal resting state, $R_a$ should be designed to be between 80 $k\Omega$ and 100 $k\Omega$. The first design requirement for implementing PAAC of biological neurons has been achieved.

To meet the second design requirement, it is necessary to understand the relationship between the remaining current of the battery and the output voltage. Conventional batteries tend to decrease output voltage when the remaining charge is low [44], while the resting potential of neuronal circuits is primarily regulated by a DC voltage source $V_T$. Therefore, we simply need to forego the use of a voltage regulator for the DC voltage source $V_T$ and allow its output voltage to decrease as the battery charge decreases. This will meet the second design requirement for implementing the PAAC of biological neurons. The third design requirement will be discussed in the next section.

Cell membrane and the non-voltage-gated, normally open ion channels attached to the cell membrane surface can be simulated using a combination of capacitors and resistors, as shown in Fig. 2. In the nervous system of higher vertebrates, the myelin sheath is a crucial cellular structure that wraps around axons. Its primary functions include isolating the axon from interference by other neurons, altering signal transmission speed, and influencing the conditions for action potential initiation. Myelin sheath holds tremendous significance in establishing stable neural circuits and processing information rapidly [18]. One might consider using a combination of voltage-controlled resistors and voltage-controlled capacitors to simulate the growth process of the myelin sheath, enabling greater adaptability and plasticity in biomimetic neurons. This paper primarily discusses the PAAC in biological neurons, only providing a dynamics model of neurons equipped with myelin sheath functionality. In this paper, the values of $R_T$ and $C_i$ $(i = 1, 2, 3)$ are directly adjusted to simulate neurons with different degrees of myelination, analyzing the impact of myelination on the power consumption of neurons.

## 3.2 Dynamics of PANCS

To establish a dynamics model of neurons based on Kirchhoff's law, it is essential to understand how neurons exchange substances, especially ions and charged particles, with the external environment. Neuronal substance exchange with the external environment occurs through free diffusion, specific channels (e.g., ion channels), and endocytosis and exocytosis, in order of increasing substance volume [45]. Small, uncharged particles like water molecules generally permeate cells through free diffusion. Conversely, ions and smaller charged particles pass through specific channels like ion channels. Larger charged or uncharged substances enter or exit nerve cells through endocytosis or exocytosis. However, exchanging charged particles through endocytosis and exocytosis minimally impacts neuronal action potential firing, often overlooked in establishing dynamics equations. The dynamical behavior of neuron growth processes is expressed in Eq. (5).

$$I(t) = \sum_{n} I_c(t) + \sum_{k} I_k(t), \tag{5}$$

where $I_c$ and $I_k$ respectively correspond to the capacitance effect and ion flow through ion channels.

From a biological perspective, the growth of the myelin sheath primarily manifests in changes in membrane capacitance and membrane permeability [36, 46]. Hence, we have Eq. (6).

$$\sum_{n} I_c(t) = \frac{C(t) \cdot du}{dt}, \tag{6}$$

where $u$ represents the total Nernst potential generated by the concentration difference of ions inside and outside the cell, namely MP, which is the potential difference between equipotential lines 1 and 2 in Fig. 2(b). The $C(t)$ is determined by the dynamical equation of the voltage-gated capacitor [20]. The total charge leakage from all ion channels is described by Eq. (7).

$$\begin{aligned} \sum_{k} I_k(t) =& g_{Na} \cdot (u - E_{Na}) + g_K \cdot (u - E_K) + g_{Ca} \cdot (u - E_{Ca}) + \\ & g_A \cdot (u - E_{Na}) + g_T \cdot (u - E_T)). \end{aligned} \tag{7}$$

The decrease in membrane permeability caused by myelination is mainly reflected in the reduction of the number of non-voltage-gated ion channels in the axon. In Eq. (7), $g_T$ denotes changes in conductance in other non-voltage-gated ion channels, while $E_T$ symbolizes their Nernst potentials. Parameters $g_{Na}$, $g_K$, and $g_{Ca}$ represent the conductance of $Na^+$, $K^+$, and $Ca^{2+}$ channels during AP generation. $E_{Na}$, $E_K$, and $E_{Ca}$ are Nernst potentials due to ion concentration gradients inside and outside the nerve cell. $g_A$ stands for AMPAR ion channel conductance. As it allows various cations, mainly $Na^+$, the Nernst potential for $g_A$ is represented by $E_{Na}$. These parameters are determined by each ion channel's dynamical equations.

Notably, as myelin sheath grows, $C(t)$ decreases, and $g_T$ increases, both irreversibly. This phenomenon showcases the growth traits of the PANCS. The variation in $g_A$ based on MP changes demonstrates the significance of PAAC in PANCS. In the biological neural system, no external charges are injected into cells ($I(t) = 0$ in Eq. (5)). By substituting Eq. (6) and (7) into Eq. (5), we derive the PAN model shown in Eq. (8). Therefore, we have achieved the third requirement of obtaining neuronal PAAC.

$$\begin{aligned} -\frac{C(t) \cdot du}{dt} =& g_{Na} \cdot (u - E_{Na}) + g_K \cdot (u - E_K) + g_{Ca} \cdot (u - E_{Ca}) \\ & + g_A \cdot (u - E_{Na}) + g_T \cdot (u - E_T). \end{aligned} \tag{8}$$

What is important to note is that Eq. (8) describes the dynamics of postsynaptic membrane receiving neurotransmitters, but lacks the description of presynaptic membrane releasing neurotransmitters' dynamics and synaptic plasticity.

From a physiological perspective, $Na^+$, $K^+$, $Ca^{2+}$ ion channels, and leak channels (non-voltage-gated, always-open $K^+$ ion channels) function more like threshold switches, which form the physiological basis for neuronal spike emission. They do not have the plasticity required to influence changes in neural network weights. Therefore, in Eq. (8), $g_{Na}$, $g_K$, $g_{Ca}$ and $g_T$ are not the sources of plasticity and adaptability.

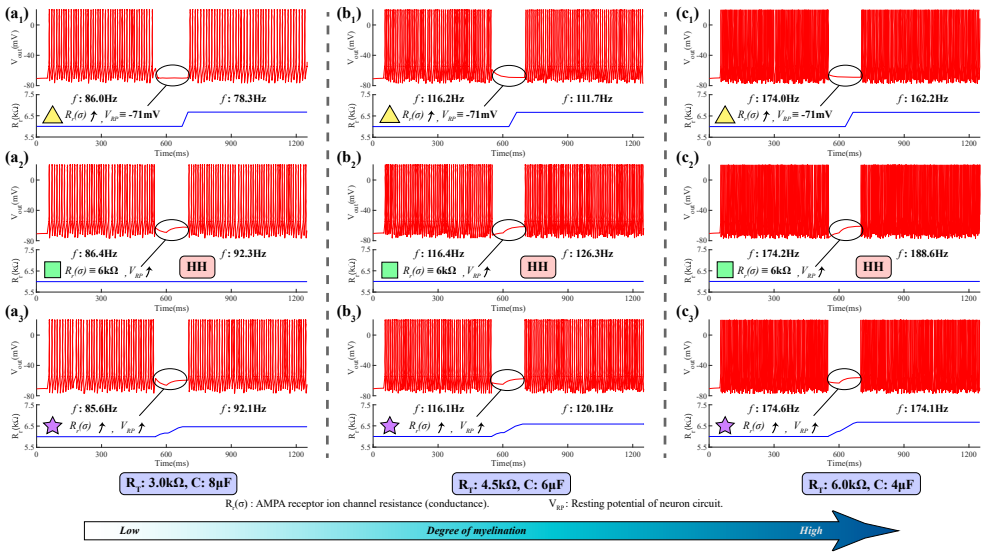


**Fig. 3** PAAC of neuron nodes with varying degrees of myelination. (a) Low-Myelination PANCS; (b) Moderate-Myelination PANCS; (c) High-Myelination PANCS

In biological neuron systems, plasticity and adaptability primarily stem from changes in synaptic weight, which involve the increase or decrease in the number of AMPA receptor ion channels, as well as myelin growth. Therefore, in PAN, i.e., Eq. (8), the regulation of plasticity and adaptability relies on parameters $C(t)$ and $g_A$.

# 4 Simulation of PANCS

In this section, firstly, we will primarily focus on discussing whether PANCS can achieve a neuron-like PAAC similar to biological neurons based on simulation results. Secondly, we will calculate the energy consumption of PANCS with different degrees of myelination and discuss the relationship between PAAC and the degree of myelination. Thirdly, We will conduct noise experiments to analyze the effects of PAAC and myelination on spike firing characteristics of PANCS.

## 4.1 PAAC of PANCS

In this section, for all physical substitution of organelles, we create a *PSpice* circuit model using dynamical equations from the previous section. We build an PANCS based on neuron structure and simulate it in *PSpice* to verify PAAC. Fig. 2(b) displays the circuit schematic, while simulation results are shown in Fig. 3. Refer to Table 1 for circuit parameters used in Fig. 2(b). All neuronal circuits are based on the dynamical model Eq. (8), thus we have fulfilled the third requirement of obtaining neuronal PAAC. The first and second design requirements are explained one by one through simulation result Fig. 3.

**Table 1** Parameters of Ion Channel Memristors.

| ID | Ion CH | $R_{off}$ | $R_{on}$ | $V_{th1}$ | $V_{th2}$ | $V_{th3}$ | $V_{th4}$ | a | $b_1$ | $b_2$ | p | $k_{on}$ | $q_1$ | $q_2$ | Dynamical Eq. |
|---|---|---|---|---|---|---|---|---|---|---|---|---|---|---|---|
| 1 | $Na^+$ CH | $1M\Omega$ | $200\Omega$ | $+\infty$ | $-110mV$ | $-119.5mV$ | $-\infty$ | 1 | 15 | 2 | 4 | 2 | 1 | 1 | (1), (2), (3) |
| 2 | $K^+$ CH | $1M\Omega$ | $20\Omega$ | $97mV$ | $7mV$ | – | – | 1 | 18 | −9.8 | 4 | 2 | 1.05 | −0.51 | (1), (3), (4) |
| 3 | $Ca^{2+}$ CH | $1M\Omega$ | $10k\Omega$ | $+\infty$ | $-195mV$ | $-120mV$ | $-\infty$ | 1 | 7 | 5 | 1.2 | 2 | 1 | 1 | (1), (2), (3) |
| 4 | AMPAR($R_r$) CH | $18K\Omega$ | $6k\Omega$ | $-7.1mV$ | $-9mV$ | $-6mV$ | $-10.3mV$ | 1 | 10 | – | 1.2 | – | 1 | – | (1), (3), (5) |

Note1 : In all memristors, the value of $k_{off}$ is 2. $V_{Na} = 55mV$, $V_{Na} = -77mV$, $V_{Ca} = 122mV$, $V_T = -71mV$, $V_r = 55mV$, $V_{KT} = 2V$, $R_a = 100k\Omega$.

In Fig. 3, we have presented neuronal firing characteristics at three different degrees of myelination, with degree of myelination increasing from left to right, namely $a_i$ to $c_i$ $(i = 1, 2, 3.)$. Fig. 3 $(a_1)$, $(b_1)$ or $(c_1)$ primarily verifies impact of changes in AMPA receptor ion channel conductance $R_r(\sigma)$ on discharge characteristics of PANCS. Fig. 3 $(a_2)$, $(b_2)$ or $(c_2)$ primarily verifies effect of resting potential $V_{RP}$ increase on the discharge characteristics of PANCS. Fig. 3 $(a_3)$, $(b_3)$ or $(c_3)$ primarily validates the PAAC of PANCS, which examines whether PANCS has the ability to maintain or reduce changes in spike firing rates when both $R_r(\sigma)$ and $V_{RP}$ are varied simultaneously.

Observing Fig. 3$(a_1)$, $(b_1)$ or $(c_1)$, we can conclude that when the resting potential V is maintained constant, an increase in the activation resistance value $R_r$ of the AMPA receptor ion channel leads to a decrease in neuronal firing frequency, consistent with mechanism of biological neurons. However, in the simulated experiments depicted in Fig. 3$(a_1)$, $(b_1)$ or $(c_1)$, the value of $R_r$ is artificially adjusted and does not vary according to the MP changes, thus failing to validate the first requirement of neuronal circuit PAAC design. Observing Fig. 3$(a_3)$, $(b_3)$ or $(c_3)$, When we set up the memristor parameters according to the values provided in the fourth row of Table 1, and the value of $R_r$ can vary with the changes in MP, combined with the conclusions obtained from the analysis of the Fig. 3$(a_1)$, $(b_1)$ or $(c_1)$, we can conclude that PANCS meets the first requirement of neuronal circuit PAAC design.

Observing Fig. 3$(a_2)$, $(b_2)$ or $(c_2)$, when we keep $R_r$ constant and adjust $V_r$ to increase the membrane potential, we observe that the discharge frequency of PANCA increases, consistent with the PAAC mechanism of biological neurons. Additionally, as mentioned earlier, the output voltage of the DC power supply decreases as the remaining charge decreases [44]. When the power supply of the mobile device is insufficient, $V_r$ will inevitably decrease, thereby reducing the resting potential of PANCA, fulfilling the second requirement of neuronal circuit PAAC design.

Observing Fig. 3$(a_3)$, $(b_3)$ or $(c_3)$, When both $V_r$ and $R_r$ increase simultaneously, the spike firing frequency of PANCA can be gradually restored, and with the increase in the degree of myelination of PANCA, it can even be fully maintained to the spike firing frequency when energy supply is insufficient. From the results, the effects of $R_r(\sigma)$ and $V_{RP}$ on the discharge characteristics of PANCS offset each other, allowing PANCS to maintain its original spike emission frequency even when energy supply is insufficient. The stable spike firing frequency of neuronal circuit nodes is one of the necessary conditions to ensure the basic operation of a neuromorphic network. Maintaining the stable spike firing frequency of node circuits under insufficient energy supply is one of the signs that demonstrate the strong robustness of neuromorphic networks.

One point to note is that the simulation results of HH circuits with different degrees of myelination are completely consistent with those shown in the Fig. 3($a_2$), ($b_2$) or ($c_2$). This implies that regardless of the degree of myelination, when MP increases, neuronal circuit nodes designed based on the HH model will inevitably experience spike frequency disorders. This will lead to a decline in the performance of neural morphology networks based on HH neuronal circuit node design, or even collapse. Additionally, excessively high spike firing frequencies will also increase node energy consumption, which is not conducive to extending the battery life of mobile smart devices.

## 4.2 Power consumption evaluation of PANCS

The impact of PANCS discharging on power consumption calculation is significant. Therefore, as shown in the Fig. 4(a), it is necessary to divide the power consumption calculation into two stages: "resting stage ($t_0$, $t_1$)" and "spiking stage($t_1$, $t_6$)," based on whether PANCS is firing. During the resting phase, the entire PANCS is in a steady state, and its power can be calculated using the conventional power calculation Eq. 9.

$$P = \frac{(u - V_r)^2}{R_a + R_r} + \frac{(u - V_T)^2}{R_T} + \frac{(u - V_{Na})^2}{R_{Naoff}} + \frac{(u - V_K)^2}{R_{Koff}} + \frac{(u - V_{Ca})^2}{R_{Caoff}}, \tag{9}$$

where $P$ represents the power of PANCS during the resting stage, and $u$ represents MP of PANCS at resting state. $R_{Naoff}$, $R_{Koff}$ and $R_{Caoff}$ respectively represent the high resistance values of the corresponding memristors. Remaining parameters correspond one-to-one with those in Fig. 2.

Spiking stage is a relatively complex process. During this stage, the power of PANCS varies with the change in MP, so we can only calculate its average power. Calculating the average power requires determining the total energy consumed and the duration of spiking stage. Because PANCS contains memristors, the resistance of each branch also varies with MP, affecting its power. Therefore, we must divide spiking stage into five time zones according to the variation pattern of the memristor, calculate the energy consumption separately for each zone, and then sum them up. As shown in Fig. 4, The five intervals are ($t_1$, $t_2$), ($t_2$, $t_3$), ($t_3$, $t_4$), ($t_4$, $t_5$) and ($t_5$, $t_6$), and their energy consumption is calculated according to Eq. 10. The total energy consumption during the spiking phase, i.e., the energy required $Q$ for PANCS to fire one spike and the average power consumption $P_m$, is also calculated according to Eq 10.

Results of power consumption calculation are shown in Fig. 4(b), (c) and (d), where we respectively mark the power consumption calculation results of PANCS with different degrees of myelination in red, blue, and green, with the degree of myelination increasing sequentially. During the resting stage, the power consumption of PANCS is as shown in Fig. 4(b). Analyzing this graph, we can conclude that as MP increases, the power consumption of PANCS decreases. As the degree of myelination of PANCS increases, the initial power consumption of PANCS decreases. However, as MP increases, its power consumption gradually becomes similar. This is because myelination primarily affects the resistance value of the non-voltage-gated potassium

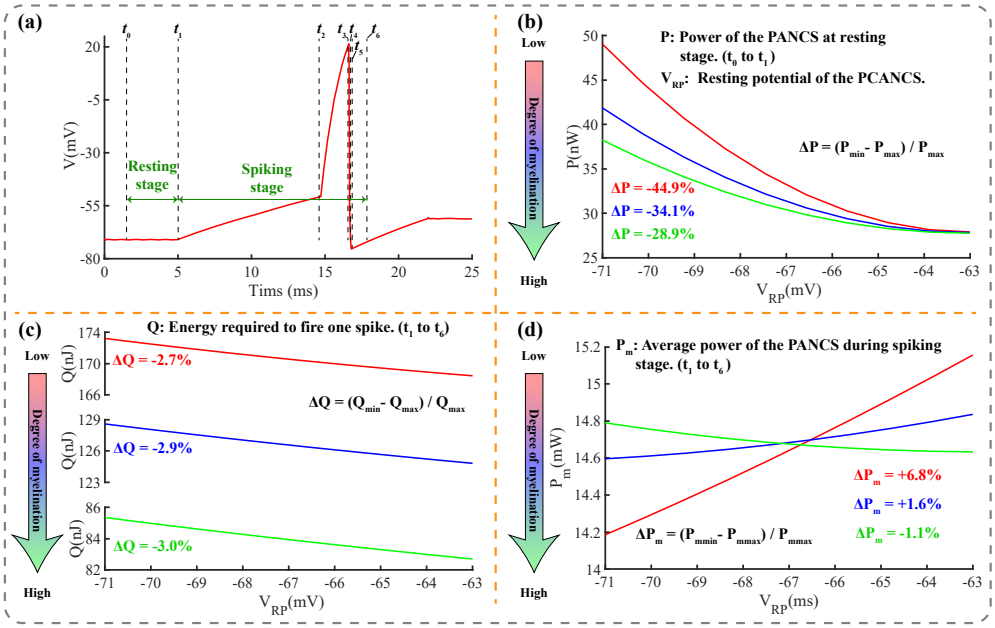


**Fig. 4** (a) Different stages of PANCS; (b) Power of PANCS at resting stages; (c) The energy consumption required for PANCS to fire a spike.; (d) Average power of PANCS at spiking stages.

ion channel $R_T$ (branch 'b' in Fig. 2(b) ), while the resistance values of other channels are much larger than $R_T$. As MP increases, the current flowing through $R_T$ tends to zero, resulting in equal total power consumption P during the resting phase for PANCS with different degrees of myelination.

$$
\begin{cases}
Q_1 = \int_{t_1}^{t_2} \dfrac{(u(t)-V_r)^2}{R_r} + \dfrac{(u(t)-V_T)^2}{R_T} + \dfrac{(u(t)-V_{Na})^2}{R_{Naoff}} + \dfrac{(u(t)-V_K)^2}{R_{Koff}} \\
\qquad + \dfrac{(u(t)-V_{Ca})^2}{R_{Caoff}}\,dt \\
Q_2 = \int_{t_2}^{t_3} \dfrac{(u(t)-V_r)^2}{R_r+R_a} + \dfrac{(u(t)-V_T)^2}{R_T} + \dfrac{(u(t)-V_{Na})^2}{R_{Naon}} + \dfrac{(u(t)-V_K)^2}{R_{Koff}} \\
\qquad + \dfrac{(u(t)-V_{Ca})^2}{R_{Caoff}}\,dt \\
Q_3 = \int_{t_3}^{t_4} \dfrac{(u(t)-V_r)^2}{R_r+R_a} + \dfrac{(u(t)-V_T)^2}{R_T} + \dfrac{(u(t)-V_{Na})^2}{R_{Naon}} + \dfrac{(u(t)-V_K)^2}{R_{Kon}} \\
\qquad + \dfrac{(u(t)-V_{Ca})^2}{R_{Caoff}}\,dt \\
Q_4 = \int_{t_4}^{t_5} \dfrac{(u(t)-V_r)^2}{R_r+R_a} + \dfrac{(u(t)-V_T)^2}{R_T} + \dfrac{(u(t)-V_{Na})^2}{R_{Naoff}} + \dfrac{(u(t)-V_K)^2}{R_{Kon}} \\
\qquad + \dfrac{(u(t)-V_{Ca})^2}{R_{Caoff}}\,dt \\
Q_5 = \int_{t_5}^{t_6} \dfrac{(u(t)-V_r)^2}{R_r+R_a} + \dfrac{(u(t)-V_T)^2}{R_T} + \dfrac{(u(t)-V_{Na})^2}{R_{Naoff}} + \dfrac{(u(t)-V_K)^2}{R_{Koff}} \\
\qquad + \dfrac{(u(t)-V_{Ca})^2}{R_{Caoff}}\,dt \\
Q = Q_1 + Q_2 + Q_3 + Q_4 + Q_5 \\
P_m = \dfrac{Q}{t_6 - t_1}
\end{cases}
\tag{10}
$$

where, $u(t)$ represents membrane potential. $R_{Naon}$, $R_{Kon}$ and $R_{Caon}$ respectively represent the low resistance values of the corresponding memristors. Remaining parameters correspond one-to-one with those in Fig. 2.

Energy required for PANCS to fire one spike at different degrees of myelination is shown in Fig. 4(c). We can observe that as the degree of myelination increases, the energy requirement for PANCS to fire a spike shows a decreasing trend, once again confirming that myelinated structures can reduce the power consumption of neuronal circuits. Average power consumption during the peak phase of PANCS with different degrees of myelination is shown in Fig. 4(d). We can clearly see that the red curve, representing the power consumption of PANCS with the lowest degree of myelination, increases with the increase of MP, but PAAC remains effective, and power consumption continues to decrease.

In low myelination PANCS, the increase in $P_m$ with the increase of MP is due to frequency disorder. One of the conclusions we reached when analyzing Fig. 3 is that

low myelination reduces the effectiveness of PAAC in stabilizing frequency. Therefore, even if PANCS at low myelination stage possess PAAC, when energy supply is insufficient, the spike firing rate will still increase compared to when energy supply is adequate. From the graph, we can infer that the energy requirement for pulse emission from PANCS decreases as MP increases, but it is not sufficient to compensate for the impact of spike frequency increases. Therefore, the average power consumption during the spike emission phase increases for PANCS at lower degrees of myelination. However, during this process, PAAC is effective because it effectively suppresses the excessive increase in spike firing frequency of PANCS. This conclusion can be verified by comparing 3 $(b_i)$ and $(c_i)$ $(i = 2, 3)$.

Observing Fig. 4(d), we can see that as the degree of myelination increases, the ability of PAAC to stabilize the spike firing rate improves to the extent that the spike firing frequency almost does not vary with changes in energy supply conditions. Consequently, the average power consumption of PANCS during the peak phase decreases with the increase in MP. This indicates that a stable spike firing frequency is particularly crucial for PAAC to reduce the power consumption of PANCS. Moreover, myelination can effectively enhance the effectiveness of PAAC. Additionally, myelination is also capable of reducing the power consumption of PANCS. This validates that the combination of myelination structure and PAAC can effectively reduce the power consumption of PANCS during insufficient energy supply while maintaining its stable spike firing frequency.

### 4.3 Effects of PAAC and myelination on spike firing characteristics of PANCS.

To further clarify the effects of PAAC and myelination on PANCS, we have designed noise experiments. In these experiments, we systematically introduce stimuli, noise, increasing MP, and other manipulations into PANCS, observing and analyzing its responses. This will help us elucidate the impacts of PAAC and myelination. Parameters of PANCS are still set according to Table 1, but to maintain the same intensity of stimulation, $R_r$ is set to $6k\Omega$. The added noise signals are set to the same intensity. Smulation results of PANCS at different degrees of myelination are shown in Fig. 5. In Fig. 5, every three rows form one group (green, purple, pink), with myelination stages increasing from top to bottom within each group. It is worth mentioning that we collected simulation results for a total of 20 seconds. However, for clarity, only the results from the first 0.35 seconds are displayed in Fig. 5. In the simulation, $V_T$ is adjusted to make $V_{RP}$ rise, with $V_T$ increasing by a value of $8mV$.

In the results shown in the first column of Fig. 5, we continuously activated the MOSFETs $T_r$ in PANCS with different degrees of myelination, adding the same stimulus to fire continuous spike signals. Analyzing the figure, we can observe that as the degree of myelination increases, the frequency of spike sequences emitted by PANCS also increases. This indicates another crucial impact of myelination, apart from reducing power consumption, which is the increases of spike frequency. The fundamental reason for both the increase in frequency and the decrease in power consumption is the same: myelination enables PANCS to lower the threshold for spike emission, making the entire circuit node more active. Compared to low myelination stages, even small

stimuli are sufficient to trigger spike firing in PANCS at highly myelinated stages. Comparing the first column of different groups leads to a conclusion that the variation in $R_T$ does not have a significant impact on the frequency, to the extent that it is not clearly observable from Fig. 5. This is because the entire PANCS can be regarded as a large-scale RC circuit, where the influence of $R_T$ on its time constant is less significant compared to $C_i$ $(i = 1, 2, 3)$. One crucial point is that in the circuit structure of PANCS, as $R_T$ increases, the total resistance between EL1 and EL2 also increases. Consequently, the influence of external noise on the discharge characteristics of PANCS will decrease. This aspect aligns with the physiological function of the myelin sheath.

In the simulations shown in the second column of Fig. 5, we discontinued the stimulation to PANCS but introduced a noise signal. Analyzing this column of the figure reveals that, under the same noise intensity, as the degree of myelination increases, the response curve of PANCS becomes thicker, indicating increased sensitivity to noise. This once again demonstrates that myelination can reduce conditions for PANCS to fire spikes, making it more responsive. However, even so, PANCS did not fire spikes due to noise. As shown in the third column of Fig. 5, when we adjusted $V_T$ to raise the resting potential $V_{RP}$, the situation changed. When $V_{RP}$ increasing, PANCS firing spikes implies lowered firing conditions, rendering it highly active, such that even slightly intense noise can fire spike. Reason is that the gap between the resting potential $V_{RP}$ and the firing threshold $V_{th}$ has decreased. This means that slightly stronger noise can elevate PANCS's MP above $V_{th}$, thereby firing spike. When the energy supply is insufficient, $V_{RP}$ inevitably rises, triggering the action of PAAC. Increasing in $V_{RP}$ implies a decreased ability of PANCS to resist noise.

The results of the three sets of experiments in the third column of Fig. 5 show that with the increase of $R_T$, even under larger conditions of $C_i$ $(i = 1, 2, 3)$, noise of equal intensity can still induce PANCS to emit sharp peaks. This proves that $R_T$ indeed can alter the time constant, thereby reducing the conditions for PANCS firing spikes. In the simulation depicted in the fourth column of Fig. 5, we simultaneously introduced noise and stimulation while increasing $V_{RP}$ of PANCS. To facilitate comparison with the results provided in the first column, we introduced the joint inter-spike interval (JISI) analysis. In Fig. 5, the fifth column represents the JISI analysis results of the first column, while the sixth column represents the JISI analysis results of the fourth column. In the JISI analysis results graph, the degree of dispersion of the scatter points is positively correlated with the extent of noise influence on PANCS. We calculate the degree of dispersion of the scatter points using equation Eq. (11). ER represents the degree of dispersion of the scatter points.

$$ER = \frac{\sum_n^i \sqrt{(x(i) - x_m)^2 + (y(i) - y_m)^2}}{n}, \tag{11}$$

where $x(i)$ and $y(i)$ respectively represent set of abscissa and ordinate of the scatter plot, $x_m$, $y_m$ represent the median.

Observing the fifth column of Fig. 5, it can be seen that without noise, the intervals between consecutive pulses emitted by PANCS are relatively regular, with fluctuations occurring within a small range. The scatter plot in the JISI graph forming a square shape also confirms the regularity of pulse emission intervals. As the myelination

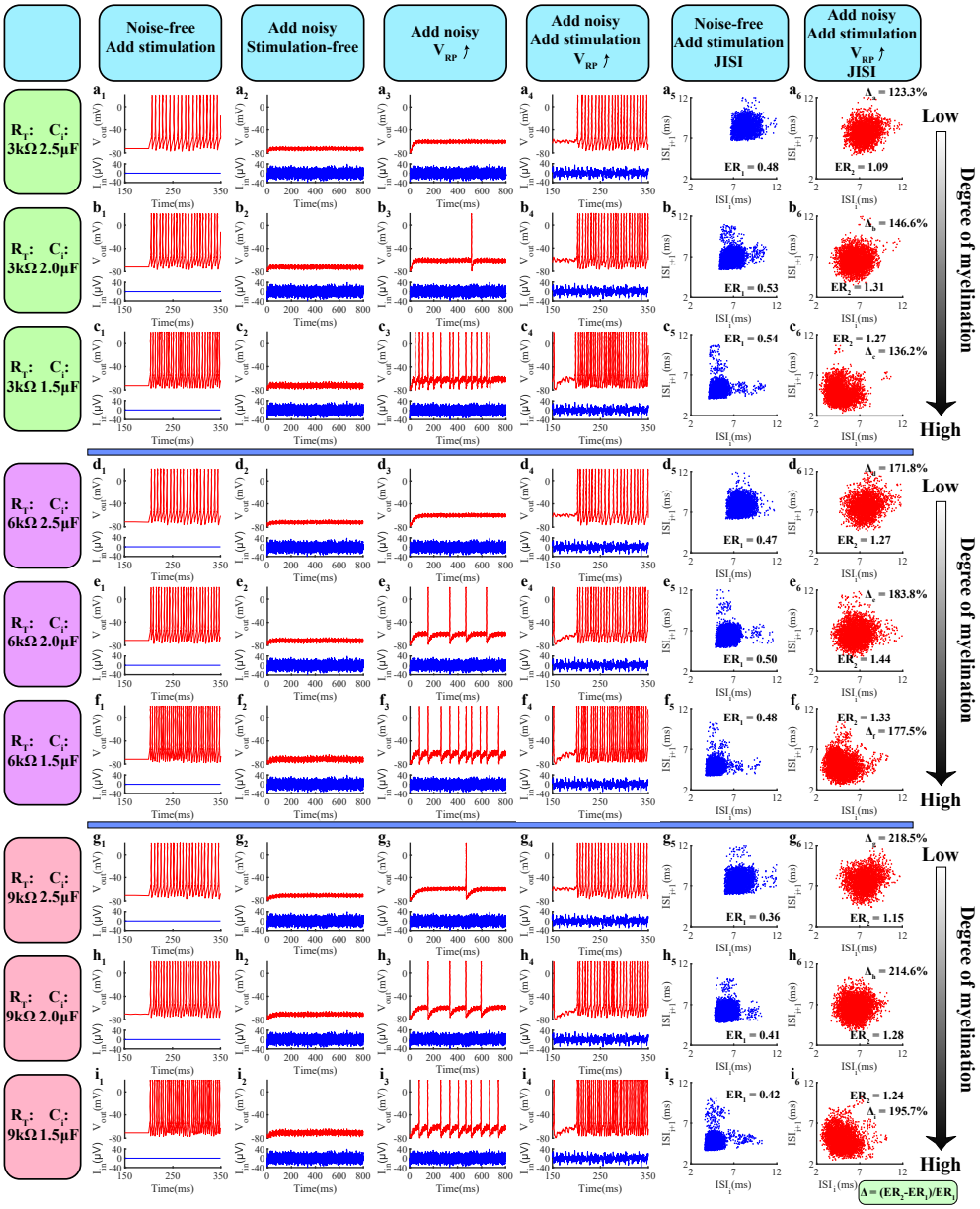


**Fig. 5** Effect of PANCS's PAAC in noisy environments $a_i$, $b_i$, $c_i$, $d_i$, $e_i$, $f_i$, $g_i$, $h_i$, $i_i$ $(i = 1, 2, 3, 4)$ and JISI test $a_i$, $b_i$, $c_i$, $d_i$, $e_i$, $f_i$, $g_i$, $h_i$, $i_i$ $(i = 5, 6)$.

degree of PANCS increases, the emission frequency rises, and the square formed by the scatter points moves towards the lower-left direction while shrinking in area. This indicates that myelination contributes to stabilizing the emission frequency of PANCS. As mentioned earlier, a stable emission frequency is a necessary condition for reducing the power consumption of PANCS when energy supply is insufficient.

As shown in the sixth column of Fig. 5, when noise is added and $V_{RP}$ is increased, the intervals between consecutive pulses emitted by PANCS become irregular, and the range of fluctuations increases. The scatter plot in the JISI graph also changes from a relatively regular square shape to an irregular pattern. Under the dual influence of noise and the increase in $V_{RP}$, the function of myelination in stabilizing pulse emission frequency becomes ineffective. Analysis of the numerical value of ER indicates that both noise and the increase in $V_{RP}$ have a significant impact on PANCS with different degrees of myelination, causing the scatter distribution of JISI points to almost reach the same level. Impact is noticeably greater on PANCS with higher degrees of myelination.

In summary, firstly, PAAC can stabilize the emission frequency of PANCS and reduce power consumption when energy supply is insufficient. Secondly, myelination can significantly reduce PANCS power consumption while also regulating spike emission rates. Thirdly, myelination can enhance the effectiveness of PAAC, further stabilizing frequency and reducing power consumption. However, as the remaining energy is further depleted, and $V_{RP}$ rises to system limits (which are negatively correlated with the background noise intensity), both PAAC and myelination become ineffective.

# 5 Practical experiments

We conducted practical experiments to verify PANCS's PAAC. Due to the exploratory nature of this work, memristor models mimicking neuronal organelles rely on biological traits. Given the absence of mature and reliable commercial memristors, we replaced them with memristor circuits in our practical experiments.

## 5.1 Experiment setting

We built a continuous signal acquisition setup using *LabVIEW* software to collect ongoing spike signals. An NI USB-6002 data acquisition card was utilized for signal sampling within the frequency range of $0Hz$ to $100Hz$. Adhering to the Shannon sampling theorem, we set the sampling rate at $50kHz$. Fig. 6 displays both the signal acquisition platform and the acquisition card.

In Fig. 7(a), 7(b), or 7(c), the memristor circuit relies on bidirectional controllable silicon properties and gate-controlled circuit design. Parameters for this circuit are detailed in Table 2. For our practical experiments, we constructed the circuit following the schematic in Fig. 2(a). We replaced $Na^+$, $K^+$, and $Ca^{2+}$ channel memristors with the circuit shown in Fig. 7. To achieve stable outputs at different MPs, we substituted memristor $R_r$ with a regular resistor $R_r^*$ whose resistance value was calculated based on MP values using Eq. (12).

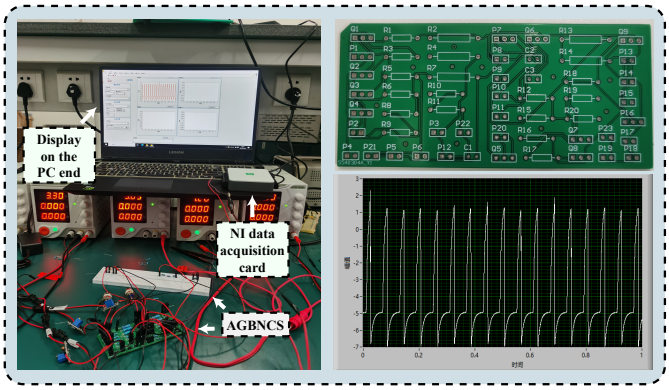


**Fig. 6** Practical experimental scenario.

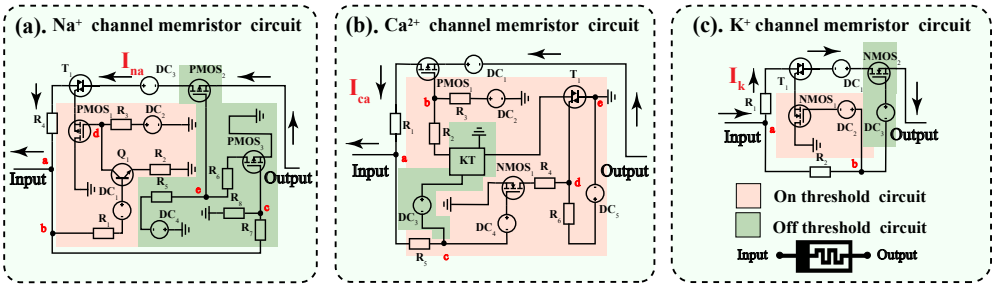


**Fig. 7** (a) Sodium ion channel memristor circuit; (b) Calcium ion channel memristor circuit; (c) Potassium ion channel memristor circuit.

**Table 2** Parameters of memristor circuit.

| Category | $R_1$ | $R_2$ | $R_3$ | $R_4$ | $R_5$ | $R_6$ | $R_7$ | $R_8$ | $DC_1$ | $DC_2$ | $DC_3$ | $DC_4$ | $DC_5$ |
|---|---|---|---|---|---|---|---|---|---|---|---|---|---|
| $Na^+$ CH circuit | $2M\Omega$ | $0.1M\Omega$ | $1M\Omega$ | $0.2k\Omega$ | $10k\Omega$ | $1k\Omega$ | $1.11M\Omega$ | $0.39M\Omega$ | $6.3V$ | $4V$ | $5.5V$ | $5.8V$ | - |
| $K^+$ CH circuit | $5\Omega$ | $2M\Omega$ | - | - | - | - | - | - | $7.7V$ | $2.5V$ | $8.5V$ | - | - |
| $Ca^{2+}$ CH circuit | $10k\Omega$ | $10\Omega$ | $100\Omega$ | $10\Omega$ | $2M\Omega$ | $50\Omega$ | - | - | $11.8V$ | $15V$ | $13V$ | $15V$ | $5V$ |

Note1 : $R_a = 100k\Omega$, $R_T = 6k\Omega$, $C_i(i = 1, 2, 3) = 4.7\mu F$.

$$R_r^* = \frac{V_{th2} \cdot R_a}{u - V_r - V_{th2}}, \tag{12}$$

where, $V_{th2}$ represents the threshold of memristor $R_r$, $R_a = 100k\Omega$. The $u$ represents the membrane potential.

A significant point to note: PANCS, like biological neurons, employs receptor ion channel branches to internally introduce positive charges, raising MP and initiating APs. In principle, as long as the resistance $R_r^*$ in branch 'a' of Fig. 2(b) and the DC voltage source $V_r$ remain constant, the charge injected into PANCS per unit

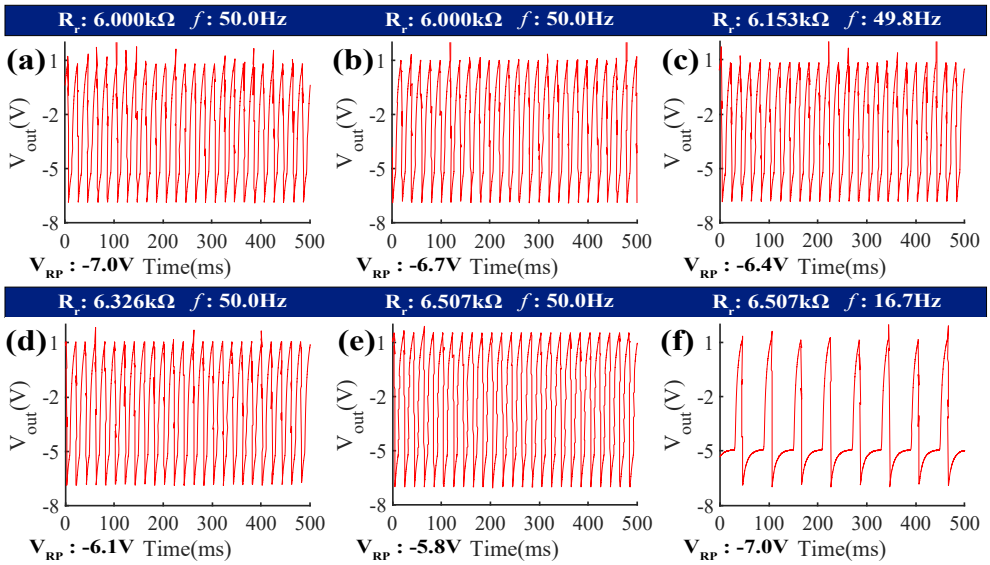


**Fig. 8** Spike firing rate of PANCS at different membrane potentials.

time through branch 'a' remains consistent. This forms the foundation for comparing different practical experiments.

### 5.2 Practical experiment analysis

The practical experiment results in Table 2 are visualized in Fig. 8. From Fig. 8, it is clear that as the membrane potential increases, the conductivity of R decreases, and the peak firing rate of PANCS settles at 50Hz. This validates PANCS's ability to maintain a steady firing rate despite adaptive changes in energy consumption.

Notably, in Fig. 8(a) to (b), with constant $R_r^*$ at $6k\Omega$ and increasing MP, the firing rate holds steady at around $50Hz$. Neuronal firing speed is linked to membrane capacitance charging. This indicates PANCS's resilience to minor MP changes; even as MP rises and the demand for charge lessens to fire spikes, its impact on firing rates remains minimal. The practical circuit shows less sensitivity to small MP changes compared to simulations. This suggests that PANCS in the practical circuit is more capable of maintaining a steady firing rate during periods of insufficient energy supply. Yet, significant MP fluctuations can notably affect PANCS's firing rate. A comparison between Fig. 8(e) and 8(f) illustrates a significant difference in PANCS firing rate when membrane potentials vary by $1.2V$.

## 6 conclusion

This paper introduces an adaptive growth neuron model equipped with PAAC, alongside its circuit design, leveraging insights from neuron energy strategies, and dynamical behaviors. The process involves establishing dynamics models based on core neuron

organelles' biological traits, proposing the PAN model integrating neuron dynamics, myelination attributes, and PAAC, and building PANCS following neuron physiology. Using PSpice software, we simulate an PANCS to validate PAAC, conduct noise testing, and estimate power consumption.Simulation and practical experiments have both demonstrated that PANCS has acquired the capability of power consumption adaptive adjustment, and can maintain stable spike emission frequency when the system's energy supply is insufficient. Moreover, this capability is positively correlated with the degree of myelination of PANCS. Power consumption analysis indicates that both PAAC and myelination can reduce the power consumption of PANCS, and the effectiveness of PAAC is positively correlated with the degree of myelination. Noise experiments demonstrate that the effectiveness of PAAC requires a reduction in the robustness of PANCS, and myelination cannot mitigate the decrease in robustness. Utilizing PANCS in designing neural morphology networks can alleviate performance degradation and reduce power consumption under insufficient energy supply. This capability ensures the basic operation of mobile intelligent robots and extends battery life under extreme conditions of insufficient power supply.

In the future, we plan to enhance the PAN model by integrating synaptic biological traits and improving growth and pulse rate modulation. This refined PAN model will serve as the foundation for designing a biomimetic neuron circuit system.Our goal is to create a mechanical nervous system with growth capabilities, facilitating the development of sophisticated intelligent robots built upon this system.

**Acknowledgements.** This work is supported by the National Natural Science Foundation of China (62171182), Natural Science Foundation Project of Chongqing, Chongqing Science and Technology Commission (CSTB2022NSCQ-M SX5843), Hunan Province Graduate Research Innovation Project (CX20240452).

# Declarations

- Funding: National Natural Science Foundation of China (62171182), Natural Science Foundation Project of Chongqing, Chongqing Science and Technology Commission (CSTB2022NSCQ-M SX5843), Hunan Province Graduate Research Innovation Project (CX20240452).
- Conflict of interest/Competing interests: The authors declare no competing interests
- Ethics approval and consent to participate
- Consent for publication
- Data availability
- Materials availability
- Code availability
- Author contribution

If any of the sections are not relevant to your manuscript, please include the heading and write 'Not applicable' for that section.

# References


[1] Chen, J., Zhu, q.Q., Zhao, q.C., Wang, q.H.: Pzt-enabled mos2 floating gate transistors: Overcoming boltzmann tyranny and achieving ultralow energy consumption for high-accuracy neuromorphic computing. Nano Lett (2023)

[2] Guo, Z., Liu, G., Sun, Y., Zhang, Y., Zhao, J., Liu, P., Wang, H., Zhou, Z., Zhao, Z., Jia, X., Sun, J., Shao, Y., Han, X., Zhang, Z., Yan, X.: High-performance neuromorphic computing and logic operation based on a self-assembled vertically aligned nanocomposite srtio3:mgo film memristor. ACS Nano **17**, 21518–21530 (2023)

[3] Kumarasinghe, K., Kasabov, D. N nd Taylor: Brain-inspired spiking neural networks for decoding and understanding muscle activity and kinematics from electroencephalography signals during hand movements. Scientific Reports **11**(1), 2486 (2021)

[4] Jiang, C., Liu, J., Ni, Y., Qu, S., Liu, L., Li, Y., Yang, L., Xu, W.: Mammalian-brain-inspired neuromorphic motion-cognition nerve achieves cross-modal perceptual enhancement. Nature Communications **14**(1), 1344 (2023)

[5] Padamsey, Z., Katsanevaki, D., Dupuy, N., Rochefort, N.L.: Neocortex saves energy by reducing coding precision during food scarcity. Neuron **110**(2), 280–296 (2022)

[6] Longden, K.D., Muzzu, T., Cook, D.J., Schultz, S.R., Krapp, H.G.: Nutritional state modulates the neural processing of visual motion. Curr Biol **24**(8), 890–895 (2014)

[7] Herculano-Houzel, S.: Scaling of brain metabolism with a fixed energy budget per neuron: implications for neuronal activity, plasticity and evolution. PLoS One **6**(3), 17514 (2011)

[8] Harris, J.J., Jolivet, R., Attwell, D.: Synaptic energy use and supply. Neuron **75**(5), 762–777 (2012)

[9] Sengupta, B., Stemmler, M., Laughlin, S.B., Niven, J.E.: Action potential energy efficiency varies among neuron types in vertebrates and invertebrates. PLoS Comput Biol **6**(7), 1000840 (2010)

[10] Attwell, D., Laughlin, S.B.: An energy budget for signaling in the grey matter of the brain. J Cereb Blood Flow Metab **21**(10), 1133–1145 (2001)

[11] Lehnert, F.B., Saab, A.S., Gutiérrez, R., Larebas, V., Díaz, E., Horn, M., Vargas, M., Hösli, L., Stobart, J., Hirrlinger, J., Weber, B., Barros, L.F.: Non-canonical control of neuronal energy status by the na+ pump. Cell Metabolism **29**(3), 668–6804 (2019)

[12] Lerchundi, R., Huang, N., Rose, C.R.: Quantitative imaging of changes in astrocytic and neuronal adenosine triphosphate using two different variants of ateam. Front Cell Neurosci **21**(14), 80 (2020)

[13] Barlow, H.B.: Sensory Communication, 1st edn. MIT Press Scholarship Online, Cambridge, MA (2012)

[14] Hansel, D., Sompolinsky, H.: Chaos and synchrony in a model of a hypercolumn in visual cortex. J Comput Neurosci **3**(1), 7–34 (1996)

[15] Kauffman, A.L., Ashraf, J.M., Corces-Zimmerman, M.R., Landis, J.N., Murphy, C.T.: Insulin signaling and dietary restriction differentially influence the decline of learning and memory with age. PLoS Biol **18**(5), 1000372 (2010)

[16] Placais, P.-Y., Tredern, E., Scheunemann, L., Trannoy, S., Goguel, V., Han, K.-A., Isabel, G., Preat, T.: Upregulated energy metabolism in the drosophila mushroom body is the trigger for long-term memory. Nature Communications **8**(1), 15510 (2017)

[17] Plaçais, P.Y., Preat, T.: To favor survival under food shortage, the brain disables costly memory. Science **339**(6118), 440–442 (2013)

[18] Blooijs, D., Boom, M.A., Aar, J.F., Huiskamp, G.M., Castegnaro, G., Demuru, M., Zweiphenning, W.J..E.M., Eijsden, P., Miller, K.J., Leijten, F.S.S., Hermes, D.: Developmental trajectory of transmission speed in the human brain. Nat Neurosci **26**(4), 537–541 (2023)

[19] Akaishi, T.: New theoretical model of nerve conduction in unmyelinated nerves. Front Physiol **8**, 798 (2017)

[20] Li, X., Sun, J., Ma, W., Sun, Y., Wang, C., Zhang, J.: Adaptive biomimetic neuronal circuit system based on myelin sheath function. IEEE Transactions on Consumer Electronics (2024)

[21] Yao, W., Wang, C.H., Sun, Y.C., Gong, S.Q., Lin, H.R.: Event-triggered control for robust exponential synchronization of inertial memristive neural networks under parameter disturbance. Neural Networks **164**, 67–80 (2023)

[22] Liang, Y., Zhu, Q., Wang, G., Nath, S.K., Iu, H.H., Nandi, S.K., Eliman, R.G., Glen, R.: Universal dynamics analysis of locally-active memristors and its applications. IEEE Transactions on Circuits and Systems I: Regular Papers **69**(3), 1278–1290 (2022)

[23] Liang, Y., Wang, G., Chen, G., Dong, Y., Yu, D., Iu, H.H.: S-type locally active memristor-based periodic and chaotic oscillators. IEEE Transactions on Circuits and Systems I: Regular Papers **67**(12), 5139–5152 (2020)

[24] Pickett, M.D., Medeiros-Ribeiro, G., Williams, R.S.: A scalable neuristor built with mott memristors. Nature Materials **12**(2), 114–117 (2013)

[25] Yi, W., Tsang, K.K., Lam, S.K., Bai, X., Crowell, J.A., Flores, E.A.: Biological plausibility and stochasticity in scalable vo2 active memristor neurons. Nature Communications **9**(1), 4461 (2018)

[26] Rajasekaran, S., Simanjuntak, F.M., Chandrasekaran, S., Panda, D., Saleem, A., Tseng, T.-Y.: Flexible ta2o5/wo3-based memristor synapse for wearable and neuromorphic applications. IEEE Electron Device Letters **43**(1), 9–12 (2022)

[27] Lv, J., Wang, S., Li, F., Liang, Q., Yang, M., Ma, X., Wang, H., Hao, Y.: A physically transient self-rectifying and analogue switching memristor synapse. IEEE Electron Device Letters **42**(11), 1599–1602 (2021)

[28] Liu, Q., Wei, Q., Ren, H., Zhou, L., Wang, P., Wang, C., Yin, J., Li, M.: Circular polarization-resolved ultraviolet photonic artificial synapse based on chiral perovskite. Nature Communications **14**(1), 7179 (2023)

[29] Liu, S., He, Z., Zhang, B., Zhong, X., Guo, B., Chen, W., Duan, H., Tong, Y., He, H., Chen, Y., Liu, G.: Approaching the zero-power operating limit in a self-coordinated organic protonic synapse. Adv Sci (2023)

[30] Yao, W., Gao, K., Zhang, Z.H., Cui, L., Zhang, J.: An image encryption algorithm based on a 3d chaotic hopfield neural network and random row–column permutation. Frontiers of Physics (2023)

[31] Wang, C., Tang, D., Lin, H., Yu, F., Sun, Y.: High-dimensional memristive neural network and its application in commercial data encryption communication. Expert Systems with Applications, 122513 (2023)

[32] Lin, H., Wang, C., Sun, Y.: A universal variable extension method for designing multiscroll/wing chaotic systems. IEEE Transactions on Industrial Electronics, 1–13 (2023)

[33] Wang, M., Gu, L.: Multiple mixed state variable incremental integration for reconstructing extreme multistability in a novel memristive hyperchaotic jerk system with multiple cubic nonlinearity. Chinese Physics B **33**(2), 020504 (2024)

[34] Shen, G., Zhao, D., Dong, Y., Zeng, Y.: Brain-inspired neural circuit evolution for spiking neural networks. Proc Natl Acad Sci U S A **120** (2023)

[35] Hu, Y., Zheng, Q., Jiang, X., Pan, G.: Fast-snn: Fast spiking neural network by converting quantized ann. IEEE Transactions on Pattern Analysis and Machine Intelligence **45**(12), 14546–14562 (2023)

[36] Gerstner, W., Lausanne, E.P.F.D., Kistler, W.M., Naud, R.: Neuronal Dynamics:

From Single Neurons to Networks and Models of Cognition. Cambridge University Press, ??? (2014)

[37] Protachevicz, P.R., Bonin, C.A., Iarosz, K.C., Caldas, I.L., Batista, A.M.: Large coefficient of variation of inter-spike intervals induced by noise current in the resonate-and-fire model neuron. Cognitive Neurodynamics **16**(6), 1461–1470 (2022)

[38] Li, X., Sun, J., Sun, Y., Wang, C., Hong, Q., Du, S., Zhang, J.: Design of artificial neurons of memristive neuromorphic networks based on biological neural dynamics and structures. IEEE Transactions on Circuits and Systems I: Regular Papers (2024)

[39] Izhikevich, E.M.: Which model to use for cortical spiking neurons? IEEE Transactions on Neural Networks **15**(5), 1063–1070 (2004)

[40] Trevisiol, A., Saab, A.S., Winkler, U., Marx, G., Imamura, H., Möbius, W., Kusch, K., Nave, K.-A., Hirrlinger, J.: Monitoring atp dynamics in electrically active white matter tracts. eLife **6**, 24241 (2017)

[41] Traynelis, S.F., Silver, R.A., Cull-Candy, S.G.: Estimated conductance of glutamate receptor channels activated during epscs at the cerebellar mossy fiber-granule cell synapse. Neuron **11**(2), 279–289 (1993)

[42] Yamashita, T., Ishikawa, T., Takahashi, T.: Developmental increase in vesicular glutamate content does not cause saturation of ampa receptors at the calyx of held synapse. J Neurosci **23**(9), 3633–3638 (2003)

[43] Talavera, K., Nilius, B.: Biophysics and structure-function relationship of t-type ca2+ channels. Cell Calcium **40**(2), 97–114 (2006)

[44] Yu, Q., Huang, Y., Tang, A., Wang, C., Shen, W.: Ocv-soc-temperature relationship construction and state of charge estimation for a series– parallel lithium-ion battery pack. IEEE Transactions on Intelligent Transportation Systems **24**(6), 6362–6371 (2023)

[45] Mosquera, J., García, I., Liz-Marzán, L.M.: Cellular uptake of nanoparticles versus small molecules: A matter of size. Acc Chem Res **51**(9), 2305–2313 (2018)

[46] Binczak, S., Eilbeck, J.C., Scott, A.C.: Ephaptic coupling of myelinated nerve fibers. Physica D: Nonlinear Phenomena **148**(1), 159–174 (2001)